J. Fluid Mech. (2015), *vol.* 779, *pp.* 390–410. © Cambridge University Press 2015
doi:10.1017/jfm.2015.423

Symmetry reduction of turbulent pipe flows

Francesco Fedele[1,2,†], Ozeair Abessi[3] and Philip J. Roberts[1]

[1]School of Civil and Environmental Engineering, Georgia Institute of Technology, Atlanta, GA 30322, USA

[2]School of Electrical and Computer Engineering, Georgia Institute of Technology, Atlanta, GA 30322, USA

[3]School of Civil Engineering, Babol Noshirvani University of Technology, Babol 47148-71167, Iran

(Received 20 December 2014; revised 22 April 2015; accepted 20 July 2015; first published online 17 August 2015)

We propose and apply a Fourier-based symmetry-reduction scheme to remove, or quotient, the streamwise translation symmetry of laser-induced-fluorescence measurements of turbulent pipe flows that are viewed as dynamical systems in a high-dimensional state space. We also explain the relation between Taylor's hypothesis and the comoving frame velocity U_d of the turbulent orbit in state space. In particular, in physical space we observe flow structures that deform as they advect downstream at a speed that differs significantly from U_d. Indeed, the symmetry-reduction analysis of planar dye concentration fields at Reynolds number $Re = 3200$ reveals that the speed u at which high-concentration peaks advect is roughly 1.43 times U_d. In a physically meaningful symmetry-reduced frame, the excess speed $u - U_d \approx 0.43U_d$ can be explained in terms of the so-called geometric phase velocity U_g associated with the orbit in state space. The 'self-propulsion velocity' U_g is induced by the shape-changing dynamics of passive scalar structures observed in the symmetry-reduced frame, in analogy with that of a swimmer at low Reynolds numbers.

Key words: general fluid mechanics, nonlinear dynamical systems, turbulent flows

1. Introduction

In the last decade, incompressible fluid turbulence in channel flows has been studied as chaotic dynamics in the state space of a high-dimensional system at moderate Reynolds numbers (see, for example, Gibson, Halcrow & Cvitanović 2008; Willis, Cvitanović & Avila 2013). Here, turbulence is viewed as an effective random walk in state space through a repertoire of invariant solutions of the Navier–Stokes equations (Cvitanović 2013 and references therein). In state space, turbulent trajectories or orbits visit the neighbourhoods of equilibria, travelling waves or periodic orbits, switching from one saddle to the other through their stable and unstable manifolds (Cvitanović & Eckhardt 1991, see also Cvitanović *et al.* 2012). Recent studies on the geometry of the state space of Kolmogorov flows (Chandler & Kerswell 2013) and barotropic

† Email address for correspondence: fedele@gatech.edu

atmospheric models (Gritsun 2011, 2013) give evidence that unstable periodic orbits provide the skeleton that underpins the chaotic dynamics of fluid turbulence.

In pipe flows, the intrinsic continuous streamwise translation symmetry and azimuthal symmetry make it difficult to identify invariant flow structures, such as travelling waves or relative equilibria (Faisst & Eckhardt 2003; Wedin & Kerswell 2004) and relative periodic orbits (Viswanath 2007), embedded in turbulence. These structures travel downstream with their own mean velocity and there is no unique comoving frame that can simultaneously reduce all relative periodic orbits to periodic orbits and all travelling waves to equilibria. Recently, this issue has been addressed by Willis *et al.* (2013) using the method of slices (Siminos & Cvitanović 2011; Froehlich & Cvitanović 2012; see also Rowley & Marsden 2000; Rowley *et al.* 2003) to quotient group symmetries that reveal the geometry of the state space of pipe flows at moderate Reynolds numbers. Further, Budanur *et al.* (2015) exploits the 'first Fourier mode slice' to reduce the $SO(2)$-symmetry in spatially extended systems. In particular, they separate the dynamics of the Kuramoto–Shivasinsky equation into shape-changing dynamics within a quotient or symmetry-reduced space (base manifold) and a one-dimensional (1D) transverse space (fibre) associated with the group symmetry. This is the geometric structure of a fibration of the state space into a base manifold and transversal fibres attached to it. Thus, the state space is geometrically a principal fibre bundle (e.g. Hopf 1931; Husemöller 1994; Steenrod 1999): a base or quotient manifold of the true dynamics that is not associated with a drift and has attached transverse fibres of invariant directions.

In this work, we propose a symmetry reduction for dynamical systems with translation symmetries, and apply it to symmetry-reduce the evolution of passive scalars of turbulent pipe flows. The paper is organized as follows. We first discuss the method of comoving frames for pipe flows, also referred to as the method of connections (e.g. Rowley & Marsden 2000). In particular, we explain the relation of comoving frame velocities to Taylor's (1938) hypothesis. This is followed by an experimental validation by means of two-dimensional (2D) laser-induced-fluorescence (LIF) measurements of planar dye concentration fields of turbulent pipe flows. The Fourier-based symmetry reduction scheme is then presented and applied to analyze the acquired experimental data.

2. Comoving frame velocities and Taylor's hypothesis

Consider an incompressible three-dimensional (3D) flow field $\boldsymbol{v}_0(x,\ y,\ z,\ t) = (U_0,\ V_0,\ W_0)$, where x and z are the horizontal streamwise and spanwise directions, and y the vertical axis. The flow satisfies the Navier–Stokes equations with proper no-slip boundary conditions on generic wall boundaries. Consider a 3D passive scalar field $C_0(x, y, z, t)$ advected and dispersed by $\boldsymbol{v}_0$ in accord with

$$\partial_t C_0 + \boldsymbol{v}_0 \cdot \boldsymbol{\nabla} C_0 = D_m \nabla^2 C_0 + f_0, \tag{2.1}$$

where D_m is the diffusion coefficient, and f accounts for sources and sinks. For the pair $(\boldsymbol{v}_0,\ C_0)$, $\boldsymbol{v}_0$ evolves according to the Navier–Stokes equations with no-slip at the wall boundaries and C_0 evolves according to (2.1). Assume that solutions to both equations have streamwise translation symmetry. This means that if $(\boldsymbol{v}_0, C_0)(x, y, z, t)$ is a solution so is $(\boldsymbol{v}_0, C_0)(x - \ell, y, z, t)$ for an arbitrary but fixed shift ℓ. Hereafter, the translationally invariant Navier–Stokes velocity field $\boldsymbol{v}_0$ is not required to be known or given since our approach is based on concentration measurements or observables only.

The presence of translation symmetry allows the construction of a symmetry-reduced system, which (depending on construction) is equivalent to observing the original system in a comoving frame $(x - \ell_d(t), y, z, t)$, where

$$U_d^{(3D)} = \frac{\mathrm{d}\ell_d}{\mathrm{d}t} \tag{2.2}$$

is the comoving frame velocity for 3D flows. As a first attempt, $U_d^{(3D)}$ can be chosen to minimize, on average, the material derivative:

$$\frac{\mathrm{D}C_0}{\mathrm{D}t} = \partial_t C_0 + U_d^{(3D)} \partial_x C_0, \tag{2.3}$$

namely

$$\langle (\partial_t C_0 + U_d^{(3D)} \partial_x C_0)^2 \rangle_{x,y,z} \tag{2.4}$$

is the smallest possible if

$$U_d^{(3D)}(t) = -\frac{\langle \partial_t C_0 \partial_x C_0 \rangle_{x,y,z}}{\langle (\partial_x C_0)^2 \rangle_{x,y,z}}, \tag{2.5}$$

where the brackets $\langle \cdot \rangle_{x,y,z}$ denote space average in x, y and z. In the comoving frame $(x - \ell_d(t), y, z, t)$, with $\ell_d(t) = \int_0^t U_d^{(3D)}(\tau)\,\mathrm{d}\tau$, the passive scalar appears to flow calmly, while still slowly drifting downstream (see, for example, Kreilos, Zammert & Eckhardt 2014 for a study of parallel shear flows). Only when $\mathrm{D}C_0/\mathrm{D}t = 0$, i.e. the diffusion, source and sink terms are in balance, is the flow steady in the comoving frame (Krogstad, Kaspersen & Rimestad 1998), for example travelling waves (Faisst & Eckhardt 2003; Wedin & Kerswell 2004). From (2.1), (2.5) can be written as

$$U_d^{(3D)}(t) = \frac{\langle U_0(\partial_x C_0)^2 + \partial_x C_0 V_0 \partial_y C_0 + W_0 \partial_x C_0 \partial_z C_0 - D_m \partial_x C_0 \nabla^2 C_0 - f_0 \partial_x C_0 \rangle_{x,y,z}}{\langle (\partial_x C_0)^2 \rangle_{x,y,z}}. \tag{2.6}$$

Equation (2.6) reveals that the comoving frame velocity is a weighted average of the local flow velocities, sources and sinks. For periodic boundary conditions the contribution of diffusion processes is null. From (2.5), averaging along the x and z directions only yields the comoving frame vertical velocity profile

$$U_d^{(3D)}(y, t) = -\frac{\langle \partial_t C_0 \partial_x C_0 \rangle_{x,z}}{\langle (\partial_x C_0)^2 \rangle_{x,z}}. \tag{2.7}$$

The associated speed $\widehat{U}_d$ of a Fourier mode $\widehat{C_0}(k_x, k_z, y, t)\mathrm{e}^{\mathrm{i}(k_x x + k_z z)}$ then follows as

$$\widehat{U}_d(k_x, k_z, y, t) = \frac{\mathrm{Re}\left[\mathrm{i}\partial_t \widehat{C}_0(k_x, k_z, y, t)\overline{\widehat{C_0}}(k_x, k_z, y, t)\right]}{k_x \left|\widehat{C_0}(k_x, k_z, y, t)\right|^2}, \tag{2.8}$$

where $\overline{\widehat{C_0}}$ is the complex conjugate of $\widehat{C_0}$, k_x and k_z are the streamwise and crosswise wavenumbers and $\mathrm{Re}(a)$ denotes the real part of a. Note that $\widehat{U}_d$ is the same as the convective velocity formulated by Del Álamo & Jimenez (2009) in the context of Taylor's (1938) abstraction of turbulent flows as fields of frozen eddies advected by the flow. When turbulent fluctuations are small compared to the larger-scale flow,

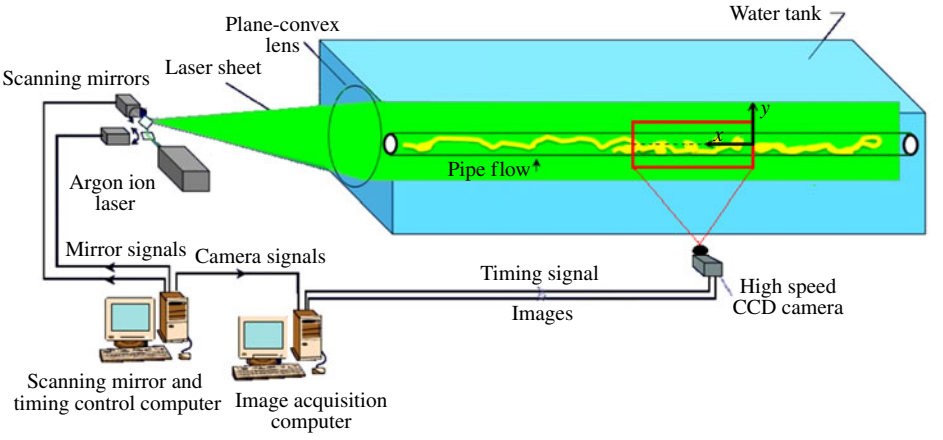

FIGURE 1. (Colour online) Schematic of the LIF system of the Georgia Tech Environmental Fluid Mechanics Laboratory (Tian & Roberts (2003), see also www.youtube.com/channel/UCg7qksJEB6spCUniij_UKzg).

they are advected at a speed very close to the time average, or mean flow velocity U_m at a fixed point. And their temporal variation at frequency ω at a fixed point in space can be viewed as the result of an unchanging spatial pattern of wavelength $2\pi/k_x$ convecting uniformly past the point at velocity $U_m = \omega/k_x$. This is Taylor's hypothesis that relates the spatial and temporal characteristics of turbulence. However, eddies can deform and decay as they are advected downstream and their speed may differ significantly from $U_d^{(3D)}$ and U_m.

In this regard, Del Álamo & Jimenez (2009) concluded that the comoving frame or convective velocity $U_d^{(3D)}$ of the largest-scale motion is close to the mean flow speed U_m, whereas it drops significantly for smaller-scale motions (Krogstad *et al.* 1998). Hence, $U_d^{(3D)}$ depends on the state of evolution of the flow. For example, it is well known that turbulent motion in channel flows is organized in connected regions of the near-wall flow that decelerate and then erupt away from the wall as ejections. These decelerated motions are followed by larger-scale connected motions toward the wall from above as sweeps. Krogstad *et al.* (1998) found that the convection velocity for ejections is distinctly lower than that for sweeps.

To gain more insight into the physical meaning of comoving frame velocities, we performed experiments to trace turbulent pipe flow patterns using non-intrusive LIF techniques (Tian & Roberts 2003) and these are discussed in the next section.

2.1. *LIF measurements*

The experiments were performed in the Environmental Fluid Mechanics Laboratory at the Georgia Institute of Technology. The LIF configuration is illustrated in figure 1 and a detailed description of the system is given in Tian & Roberts (2003). The tank has glass walls 6.10 m long $\times$ 0.91 m wide $\times$ 0.61 m deep. The front wall consists of two 3 m long glass panels to enable long unobstructed views. The 5.5 m long pipe was located on the tank floor, and the tank was filled with filtered and dechlorinated water. The pipe was a transparent Lucite tube with radius $R = 2.5$ cm.

The pipe was completely submerged in water to avoid refraction and scattering of the emitted light that would occur at the water–lucite–air interface along the pipe

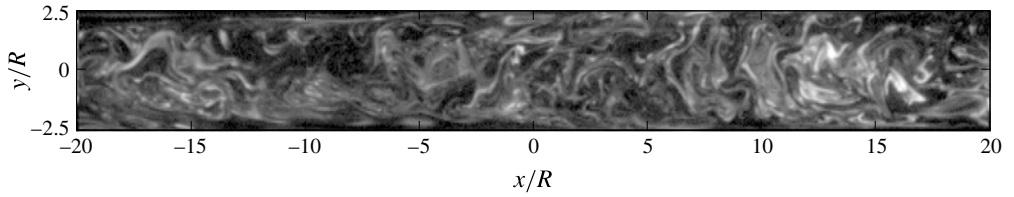

FIGURE 2. LIF experiments: snapshot of the planar fluorescent dye concentration field $C_0(x, y, z=0, t)$ tracing turbulent pipe flow patterns at Reynolds number $Re = 3200$ (bulk velocity $U_b = 6.42$ cm s^{-1}, flow from right to left).

walls and downstream at the very end of the pipe when the water flows out with curvy streamlines. With this configuration, we enable unique LIF imaging of the flow structures in a round pipe at high flow rate since the pipe discharge is into ambient water instead of air.

The water was pumped into a damping chamber to calm the flow, and then, after passing through a rigid polyester filter, it flowed into the pipe. Fluorescent dye solution was continuously injected into the flow through a small hole in the pipe wall upstream of the image capture zone of length $20R$. The solution, a mixture of water and fluorescent dye, is supplied from a reservoir by a rotary pump at a flow rate measured by a precision rotameter. The flow was started and, after waiting a few minutes for the flow to establish, laser scanning began to record the experiment. To acquire high-resolution data, we captured vertical centreline planar fluorescent dye concentration fields $C_0(x, y, z = 0, t)$ which trace turbulent pipe flow patterns. The pipe Reynolds number $Re = 2U_bR/\nu = 3200$, where the bulk velocity (discharge divided by the pipe cross-sectional area) $U_b = 6.42$ cm s^{-1} and ν is the kinematic viscosity of water. As shown in figure 1, the vertical laser sheet passes through the pipe centreline to focus on flow properties in the central plane ($z = 0$). Images of the capture zone ($2R \times 20R = 5 \times 50$ cm^2) were acquired at 50 Hz for 240 s (see figure 2). The vertical and horizontal image sizes are 65 pixel × 622 pixel for a resolution of 0.0794 cm pixel^{-1}.

2.2. *Data analysis*

The LIF measurements are planar dye concentration fields $C(x, y, t) = C_0(x, y, z=0, t)$ in a vertical slice through the pipe centreline. According to (2.1), at $z = 0$, the field C satisfies

$$\partial_t C + \boldsymbol{v}_{2D} \cdot \boldsymbol{\nabla}_{xy} C = D_m \nabla^2_{xy} C + f, \tag{2.9}$$

where $\boldsymbol{\nabla}_{xy} = (\partial_x, \partial_y)$ and $\boldsymbol{v}_{2D} = (U, V) = (U_0(x, y, z=0, t), V_0(x, y, z=0, t))$ are the in-plane gradient and flow within the 2D slice, and the source

$$f(x, y, t) = -W_0(x, y, z=0, t)\partial_z C + D_m \partial_{zz} C|_{z=0} + f_0(x, y, z=0, t) \tag{2.10}$$

accounts for the out-of-plane transport and diffusion and in-plane source/sinks. The associated in-plane comoving frame, or convective, velocity $U_d^{(2D)}$ can be estimated from the measured field $C(x, y, t)$ using (2.5), where the average is performed only in the x and y directions, that is

$$U_d^{(2D)}(t) = -\frac{\langle \partial_t C \partial_x C \rangle_{x,y}}{\langle (\partial_x C)^2 \rangle_{x,y}} = \frac{\langle \widetilde{U}(\partial_x C)^2 + \widetilde{V}\partial_x C \partial_y C - D_m \partial_x C \nabla^2_{xy} C - f \partial_x C \rangle_{x,y}}{\langle (\partial_x C)^2 \rangle_{x,y}}. \tag{2.11}$$

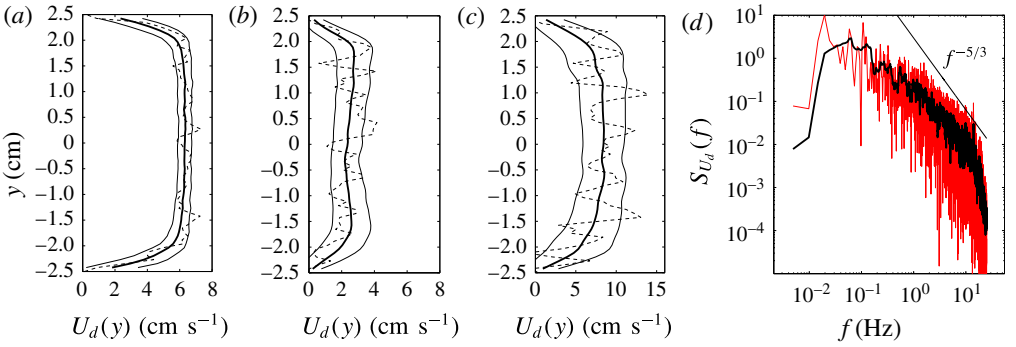

FIGURE 3. (Colour online) LIF experiments: estimated comoving frame, or convective velocity $U_d^{(2D)}(y, t)$ using (2.12): time-average profile (solid line), instantaneous profile (dashed line) and its standard deviations about the mean (thin solid lines) estimated accounting for (*a*) all spatial scales of the measured C (max speed = 6.32 cm s^{-1}), (*b*) small scales (max speed = 2.76 cm s^{-1}), (*c*) large scales (max speed = 8.52 cm s^{-1}); (*d*) observed noisy (red line) and filtered (black line) frequency spectra of the large-scale comoving frame velocity $U_d^{(2D)}$ (see (2.11)). Pipe radius $R = 2.5$ cm.

Clearly, this depends on the in-plane flow and out-of-plane sources/sinks. Similarly, the in-plane comoving frame, or convective, velocity profile $U_d^{(2D)}(y, t)$ follows from (2.7) averaging only in the x direction,

$$U_d^{(2D)}(y, t) = -\frac{\langle \partial_t C \partial_x C \rangle_x}{\langle (\partial_x C)^2 \rangle_x}. \tag{2.12}$$

For example, figure 3 shows the comoving frame velocity profiles computed from (2.12) including (*a*) all spatial scales of the measured C, (*b*) the small scales (wavelengths $L_x < 0.2R$, $L_y < 0.2R$) and (*c*) the large scales ($L_x > 2R$, $L_y > 0.4R$). Clearly, the small scales advect more slowly than the large scales, in agreement with Krogstad *et al.* (1998). Moreover, the maximum comoving frame velocity of the large scales (=8.52 cm s^{-1}) is close to the centreline mean flow speed (=8.78 cm s^{-1}) estimated from the frequency–wavenumber spectrum of $C(x, y = 0, t)$ (see figure 4). Further, the frequency spectrum of the comoving frame velocity $U_d(t)$ estimated from (2.11) accounting for large scales only is also shown in figure 3(*d*). It decays approximately as $f^{-5/3}$, indicating that Taylor's hypothesis is approximately valid, possibly due to the non-dispersive behaviour of large-scale motions.

In the fixed frame (x, t), the space–time evolution of the measured dye concentration $C(x, y = 0, t)$ on the pipe centreline is shown in figure 5(*a*). The associated evolution in the comoving frame $(x - \ell_d(t), t)$ is shown in figure 5(*b*). The shift ℓ_d is computed by numerically integrating $U_d^{(2D)}$ in time, which is estimated from (2.12) accounting for all spatial scales of C. Note the shape-changing dynamics of the passive scalar structures, which still experience a drift in the comoving frame. Moreover, a slowdown or deceleration is observed in the dye concentration peaks, possibly related to the above-mentioned turbulent flow ejections. This is clearly seen in figure 5(*c*), which depicts the normalized instantaneous peak concentration C_{peak} (normalized to C_{max}) as a function of the associated peak speed u (normalized to $U_d^{(2D)}$), with C_{max} denoting the maximum value of C over the whole 2D data set. Further, the peak speed u

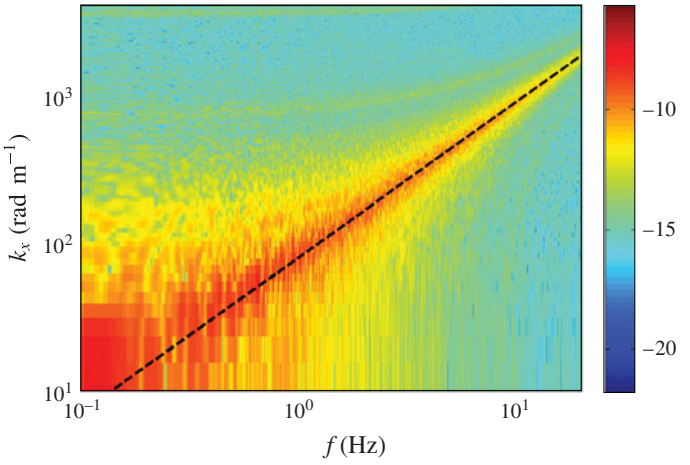

FIGURE 4. (Colour online) Observed log-values of the frequency–wavenumber spectrum $S(k_x, f)$ of the fluorescent dye concentration $C(x, y = 0, t)$ at the pipe centreline. Estimated mean flow velocity $U_m = \omega/k_x = 2\pi f/k_x \sim 8.78$ cm s^{-1} (dashed line). $U_m/U_b = 1.37$ and bulk velocity $U_b = 6.42$ cm s^{-1}.

is approximately 40 % larger than the comoving frame velocity, which is roughly constant during the event ($U_d^{(2D)} = 6.32 \pm 0.22$ cm s^{-1}). Note that in oceanic wave groups, large focusing crests tend to slow down as they evolve within the group, as a result of the natural wave dispersion of unsteady wave trains (Banner *et al.* 2014; Fedele 2014*a*,*b*). Thus, we argue that the observed slowdown of the passive scalar peaks may be due to the wave-like dispersive nature of small-scale turbulent structures.

Drawing from differential geometry, the observed excess speed $u - U_d^{(2D)}$ of concentration peaks is explained in terms of geometric phases.

3. Geometric phases

A classical example in which geometric phases arise is the transport of a vector tangentially on a sphere. The change in the vector direction is equal to the solid angle of the closed path spanned by the vector and it can be described by Hannay's angles (Hannay 1985). The rate at which the angle, or geometric phase, changes in time is the geometric phase velocity. In physics, the rotation of Foucault's pendulum can also be explained by means of geometric phases. Pancharatnam (1956) discovered their effects in polarized light, and later Berry (1984) for quantum-mechanical systems.

Consider another example drawn from classical mechanics. The dynamics of a spinning body in a dissipationless medium admits rotational symmetry with respect to the axis of rotation. The associated angular, or geometric, phase velocity Ω follows from conservation of angular momentum $I\Omega^2$, where I is the moment of inertia. Clearly, Ω can vary in time if the body shape deforms to induce changes in I. Since the body shape and its deformations are usually known, the rotation speed depends only on how the shape deforms. Indeed, in the frame rotating at the speed Ω, we only observe the body shape-changing dynamics and the rotational symmetry is 'removed' or quotiented out. We label this special frame as symmetry-reduced since in a fixed laboratory frame we cannot distinguish between the body deformation and spinning motions.

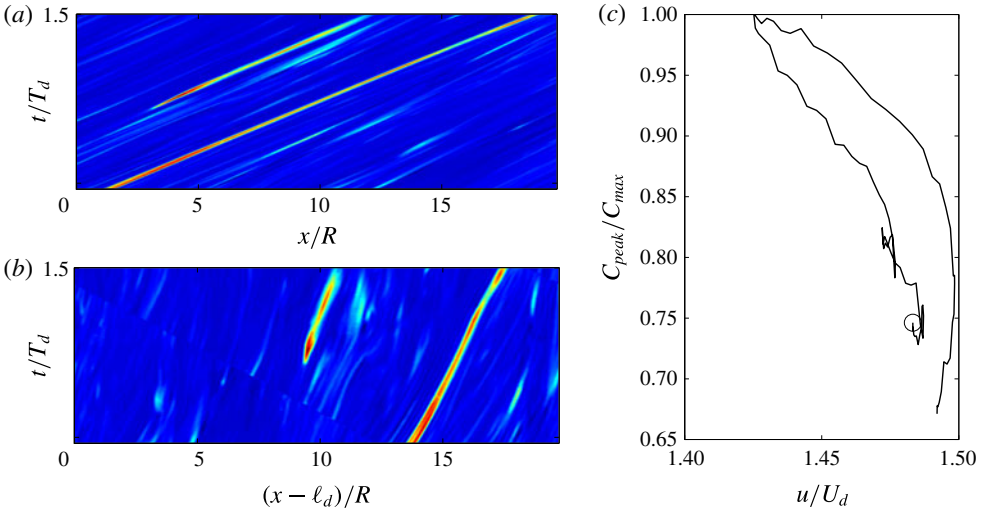

FIGURE 5. (Colour online) LIF experiments: space–time evolution of the dye concentration $C(x,\ y=0,\ t)$ at the pipe centreline in the (a) lab frame $(x,\ t)$ and (b) comoving frame $(x-x_d(t),\ t)$; (c) normalized instantaneous concentration peak intensity C_{peak}/C_{max} tracked from the initial time $t/T_d=0$ (○) as a function of the observed peak speed $u/U_d^{(2D)}$, with C_{max} denoting the observed maximum value of C over the whole data set. $U_d\approx 6.34$ m s^{-1} and $T_d=U_d/R$.

In fluid mechanics, the motion of a swimmer at low Reynolds numbers can also be explained in terms of geometric phase velocities (Shapere & Wilczek 1989). In this case, the comoving frame velocity is null since inertia is neglected and the swimmer's velocity is uniquely determined by the geometry of the sequence of its body shapes, which lead to a net translation, i.e. the geometric phase. In a fixed laboratory frame we observe the swimmer drifting as its body shape varies in time, but it is hard to distinguish between the two types of motions. In the symmetry-reduced frame moving with the swimmer we only observe its body deformations and translation symmetry is quotiented out.

In wave mechanics, the recently noticed slowdown effect of crests of oceanic wave groups can be explained in terms of geometric phase velocities (Banner *et al.* 2014; Fedele 2014*a*).

In the above-mentioned cases, the associated governing equations are linear and the shape deformations are known or assumed *a priori*. Indeed, in quantum-mechanical systems their shape depends on the eigenfunctions of the Schrödinger operator (Berry 1984). Shapere & Wilczek (1989) considered the eigenfunctions of the Stokes operator to describe the swimmer's shape. Fedele (2014*a*) considered the special class of Gaussian envelopes to study the qualitative dynamics of realistic ocean wave groups.

In turbulent pipe flows, fluctuating coherent structures advect downstream at a speed that depends on both their intrinsic properties such as inertia, and on the way their 'shape' varies or deforms in time. However, we do not know *a priori* their shape as the Navier–Stokes equations are nonlinear and one cannot rely on an eigenfunction expansion to model shapes. Clearly, one can use the eigenfunctions of the linearized Navier–Stokes operator or define a special flow given by the superposition of patches

of constant vorticity whose boundaries change in time according to given shape modes. However, these are just approximations or simplifications of the more complex turbulent flows.

In general, the speed of coherent structures includes not only the comoving frame velocity, which accounts primarily for their inertia, but also a geometric component. This can be interpreted as a 'self-propulsion' velocity induced by the shape-changing deformations of the flow structures similar to that of a swimmer at low Reynolds numbers (Shapere & Wilczek 1989).

To unveil the 'shape of turbulence' we need to quotient out the translation symmetry. This can be achieved, for example, by means of a physically meaningful slice representation of the quotient space (Cvitanović *et al.* 2012; Budanur *et al.* 2015). Slicing should provide a symmetry-reduced frame from which one observes the shape-changing dynamics of coherent structures without drift. The relative velocity between the comoving and symmetry-reduced frame is the geometric phase velocity.

Clearly, in the previous section we have seen that the comoving frame velocity of pipe flows has the physical meaning of a convective speed. The geometric phase velocity, on the other hand, depends on an arbitrary definition of the symmetry-reduced frame. Different slice representations yield different symmetry-reduced frames, as we will show later. Finding a physically meaningful symmetry-reduced frame from which one observes the shape of turbulence is still an open problem.

In the following, we first present a symmetry-reduction scheme for quotient translation symmetry using slice representations, and then we apply it to symmetry-reduce the LIF data of turbulent pipe flows presented in the previous section.

4. Symmetry reduction via slicing

As an application, we focus on the desymmetrization of the average in-plane concentration field $c(x, t) = \langle C(x, y, t)\rangle_y$. It is convenient to express c by means of the truncated Fourier series

$$\begin{aligned} c(x, t) &= c_0(t) + \frac{1}{2}\sum_{m=1}^{N} z_m(t)\exp(\mathrm{i}mk_x x) + \text{c.c.} \\ &= c_0(t) + \sum_{m=1}^{N} |z_m(t)|\cos(mk_0 x + \theta_m(t)), \end{aligned} \tag{4.1}$$

where $c_0(t)$ is the mean, $z_m = |z_m|\exp(\mathrm{i}\theta_m)$ is the complex Fourier amplitude with phase θ_m, $k_0 = 2\pi/L_0$ is a minimum possible wavenumber for the domain length L_0 of interest, and the index m runs from 1 to N. The mean c_0 is invariant under the group action, but its evolution is coupled to that of the fluctuating component of c. This depends on the evolution of the vector $\boldsymbol{z}(t) = \{z_m\} = (z_1, \ldots, z_N)$ of Fourier components of c and those of the translationally invariant Navier–Stokes velocity field $\boldsymbol{v}$, denoted by the vector $\hat{\boldsymbol{v}}$. The velocity field is not required to be given or known because the proposed symmetry reduction can be applied to concentration measurements only.

The coupled dynamics of c_0 and $\boldsymbol{z}$ can be derived by averaging the governing equation (2.9) in the y direction, applying flow boundary conditions and projecting onto a Fourier basis. Without losing generality, we can write

$$\left.\begin{aligned} \frac{\mathrm{d}\boldsymbol{z}}{\mathrm{d}t} &= \mathscr{N}_1(c_0, \boldsymbol{z}, \hat{\boldsymbol{v}}), \\ \frac{\mathrm{d}c_0}{\mathrm{d}t} &= \mathscr{N}_2(c_0, \boldsymbol{z}, \hat{\boldsymbol{v}}), \end{aligned}\right\} \tag{4.2}$$

where $\mathscr{N}_1$ and $\mathscr{N}_2$ are appropriate nonlinear operators of their arguments and both are invariant under translation symmetry, *viz.* $\mathscr{N}_k(c_0,\, g_\ell(\boldsymbol{z}),\, g_\ell(\hat{\boldsymbol{v}})) = g_\ell \mathscr{N}_k(c_0,\, \boldsymbol{z},\, \hat{\boldsymbol{v}})$. The orbit $\boldsymbol{z}$ wanders in the state space $\mathscr{P} \in \mathbb{C}^N$, and the one-parameter group orbit $g_\ell(\boldsymbol{z})$ of $\boldsymbol{z}$ is the subspace

$$g_\ell(\boldsymbol{z}) = \{\boldsymbol{w} \in \mathbb{C}^N : \boldsymbol{w} = \{z_m \exp(\mathrm{i}mk_0\ell)\},\ \forall \ell \in \mathbb{R}\}, \tag{4.3}$$

where the length ℓ is the drift. For a non-vanishing Fourier mode z_j, the symmetry-reduced or desymmetrized orbit $\boldsymbol{Z}(t)$ is defined by the complex components

$$\boldsymbol{Z} = \Pi_j(\boldsymbol{z}) = \{Z_m\} = \left\{ z_m \left(\frac{\bar{z}_j}{|z_j|} \right)^{m/j} \right\} = \{|z_m| \exp(\mathrm{i}\phi_m)\}, \tag{4.4}$$

where the phases

$$\phi_m = \theta_m - \frac{m\theta_j}{j}. \tag{4.5}$$

Note that $Z_j = |z_j|$ is real and $\boldsymbol{Z} \in \mathbb{C}^{N-1}$. For $j = 1$, the reduction scheme yields the 'first Fourier mode slice' proposed in Budanur *et al.* (2015). The scalar field c_D in the symmetry-reduced frame follows from (4.1) as

$$c_D(x,\, t) = c_0(t) + \sum_{m=1}^{N} |z_m| \cos(mk_0 x + \phi_m). \tag{4.6}$$

It is straightforward to check that any translated copy of $c(x + \ell,\, t)$ corresponds to a unique c_D. Indeed, the associated Fourier phases ϕ_m in (4.5) are invariant under the change $\theta_m \to \theta_m + m\ell$. In mathematical terms, the map Π_j projects an element $\boldsymbol{z} = \{z_m\}$ of $\mathscr{P}$ and all the elements of its group orbit $g_\ell(\boldsymbol{z})$ onto the same point $\boldsymbol{Z} = \Pi_j(\boldsymbol{z})$ of the quotient space $\mathscr{M} = \mathscr{P}/g_\ell \in \mathbb{C}^{N-1}$, i.e. $\Pi_j(\boldsymbol{z}) = \Pi_j(g_\ell(\boldsymbol{z}))$. Note that $\mathscr{M}$ has one dimension less than the original space since we have 'removed' translation symmetry. Indeed, $\mathscr{M}$ is defined as a manifold of $\mathbb{C}^N$ that satisfies $\mathrm{Im}(z_j) = 0$.

For $j > 1$, the presence of complex roots of z_m requires care in computing the components Z_m in (4.4). In particular, we define a slice as a subregion of the original state space $\mathscr{P}$ whose elements are mapped onto the quotient space $\mathscr{M}$ via the projection map Π_j. Slicing a state space is in general not unique. In this work, we consider the Fourier slice S_j of $\mathscr{P}$ defined as

$$S_j = \{\boldsymbol{z} \in \mathbb{C}^{\mathbb{N}} : z_j \neq 0\}, \tag{4.7}$$

which is a region of $\mathbb{C}^N$ delimited by, but not including, the border of S_j, i.e. the hyperplane $z_j = 0$. S_j can be divided into j wedge-shaped subregions based on the values of the phase θ_j of z_j as

$$S_j = \bigcup_{k=0}^{j-1} S_{j,k}, \tag{4.8}$$

where the subslice $S_{j,k}$ is the wedge domain defined as

$$S_{j,k} = \left\{ \boldsymbol{z} \in \mathbb{C}^N : z_j \neq 0 \text{ and } \frac{2\pi}{j}k < \theta_j < \frac{2\pi}{j}(k+1) \right\}. \tag{4.9}$$

The division into subslices is necessary because the phases ϕ_m of Z_m in (4.5) jump by $2\pi/j$ each time the orbit z_j winds around the origin of the complex plane crossing the branch cut $\{\mathrm{Re}(z_j) \in (0, -\infty)\}$. Thus, Π_j maps elements of $\mathscr{P}$ into any of the k subslices $S_{j,k}$. As z_j winds around the origin, a different $S_{j,k}$ has to be chosen to have continuity of the phases ϕ_m of Z_m. Tracking the winding number $\mathrm{Im} \oint (\mathrm{d}z_j/z_j)$ signals when one must switch to a different subslice. In a more practical way, a jump-free symmetry-reduced orbit $\boldsymbol{Z}$ is obtained by first unwrapping the phase θ_j of z_j and then computing Z_m by means of (4.4) and (4.5). As a result, Π_j is defined on the slice S_j (see (4.7)).

Within the quotient space $\mathscr{M}$, after j cycles are completed, relative equilibria reduce to equilibria and relative periodic orbits (RPOs) reduce to periodic orbits (POs). Indeed, after one cycle the projected orbit drifts by $2\pi/(jk_0)$ in physical space, and we refer to it as a modulo-$2\pi/j$ periodic orbit (MPO). Each RPO and its shifted copies are uniquely mapped to an MPO in the quotient space since the symmetry reduction is well defined. Clearly, an ergodic trajectory, which temporarily visits neighbourhoods of RPOs in full space may experience on average no drift in the desymmetrized or quotient space if the slice j is properly chosen, as will be shown later on. The practical and easy choice would be the first Fourier slice S_1. However, a good reduction requires the amplitude of z_j to be dominant in comparison to the other Fourier components. Indeed, in general as z_j lingers near zero, the orbit wanders near the border of the slice S_j. As a result, the map Π_j becomes singular since the phase θ_j is undefined (see, for example, Budanur *et al.* 2015). A different slice can then be chosen and the slices' borders can be adjoined via ridges into an atlas that spans the state space region of interest (Cvitanović *et al.* 2012).

The choice of the Fourier slice S_j to quotient out the translation symmetry is entirely arbitrary. Different slices yield different symmetry-reduced frames in which the concentration field may appear distorted. As an example, consider the state space to be an infinitely long vertical cylinder with its vertical lines fibres of the principal bundle (e.g. Husemöller 1994; Steenrod 1999). Each fibre can be associated with a single point in the quotient space. If we slice the cylinder transversally by a plane, the quotient space is an ellipse, or circle if the plane is orthogonal to the fibres. Of course, we can also slice the cylinder with a curved surface and the slice is a warped ellipse. Clearly, different slices are equivalent since slanted/warped ellipses and circles can be mapped into each other.

Thus, what is the best Fourier slice representation of turbulent pipe flow? We argue that a proper choice of the Fourier slice should provide a physically meaningful symmetry-reduced frame in which the shape-changing dynamics of coherent structures is observed without drift. In this case, the observed drift in the comoving frame is explained by means of geometric phases (see figure 5*b*). For our LIF measurements we need to resort to higher-order Fourier slices, as we will show below.

4.1. *Dynamical and geometric phases*

From (4.4), the action of the map Π_j is to shift the orbit $\boldsymbol{z}(t) = \{z_m(t)\}$ in $\mathscr{P}$ by an amount

$$\ell_s = -\frac{\theta_j}{k_0 j}, \quad j \geqslant 1, \tag{4.10}$$

and the resulting desymmetrized or sliced orbit

$$\boldsymbol{Z}(t) = g_{-\ell_s}(\boldsymbol{z}) = \{Z_m(t)\} \tag{4.11}$$

has Fourier components

$$Z_m = z_m \exp(-\mathrm{i}mk_0\ell_s), \quad m = 1, \ldots, N. \tag{4.12}$$

Note that the desymmetrized orbit $\boldsymbol{Z} = g_{-\ell_s}(z)$ does not satisfy the same dynamical equation (4.2) for z, i.e. $\mathrm{d}z/\mathrm{d}t = \mathscr{N}_1(z)$. Indeed (see appendix A),

$$\frac{\mathrm{d}\boldsymbol{Z}}{\mathrm{d}t} + \frac{\mathrm{d}\ell_s}{\mathrm{d}t} T(\boldsymbol{Z}) - \mathscr{N}_1(\boldsymbol{Z}) = 0, \tag{4.13}$$

where

$$T(\boldsymbol{Z}) = (g_\ell^{-1}\partial_\ell g)(\boldsymbol{Z}) = \{\mathrm{i}mk_0 Z_m\} \tag{4.14}$$

is the tangent space to the group orbit at $\boldsymbol{Z}$ (see, for example, Cvitanović *et al.* 2012).

It is well known that the total drift ℓ_s is the sum of dynamical (ℓ_d) and geometric (ℓ_g) phase drifts (Simon 1983; Samuel & Bhandari 1988)

$$\ell_s = \ell_d + \ell_g, \tag{4.15}$$

where

$$\ell_d = \int_0^t U_d \,\mathrm{d}\tau, \quad \ell_g = \int_0^t U_g \,\mathrm{d}\tau. \tag{4.16a,b}$$

Here, we have defined the associated dynamical (U_d) and geometric (U_g) phase velocities and the total drift speed follows as

$$U_s = \frac{\mathrm{d}\ell_s}{\mathrm{d}t} = U_d + U_g. \tag{4.17}$$

The decomposition into dynamical and geometric components of the drift ℓ_s and associated velocity follows from the condition of transversality of the symmetry-reduced trajectory $\boldsymbol{Z}$ to the group orbit $g_{\ell_s}(\boldsymbol{Z})$, that is $\mathrm{d}\boldsymbol{Z}/\mathrm{d}t$ is transversal to the group orbit tangent $T(\boldsymbol{Z})$ (Viswanath 2007; Cvitanović *et al.* 2012). Indeed, multiply both members of (4.13) by $\overline{T(\boldsymbol{Z})}$ as

$$\overline{T(\boldsymbol{Z})} \cdot \frac{\mathrm{d}\boldsymbol{Z}}{\mathrm{d}t} + \frac{\mathrm{d}\ell_s}{\mathrm{d}t} |T(\boldsymbol{Z})|^2 - \overline{T(\boldsymbol{Z})} \cdot \mathscr{N}_1(\boldsymbol{Z}) = 0, \tag{4.18}$$

where

$$\boldsymbol{a} \cdot \boldsymbol{b} = \overline{a}_p W_{pq} b_q \tag{4.19}$$

is a weighted scalar product of two vectors with weights $W_{pq} = \overline{W}_{qp}$. In this work we will use the standard scalar product and the group orbit is sliced orthogonally, i.e. $W_{pq} = \delta_{pq}$ where δ_{pq} is the Kronecker symbol.

The rate of change of the total drift ℓ_s is a real number and it follows from the real part of (4.18) as

$$U_s = \frac{\mathrm{d}\ell_s}{\mathrm{d}t} = \underbrace{\frac{\mathrm{Re}(\overline{T(\boldsymbol{Z})} \cdot \mathscr{N}_1(\boldsymbol{Z}))}{|T(\boldsymbol{Z})|^2}}_{\textit{dynamic}} + \underbrace{\frac{-\mathrm{Re}\left(\overline{T(\boldsymbol{Z})} \cdot \dfrac{\mathrm{d}\boldsymbol{Z}}{\mathrm{d}t}\right)}{|T(\boldsymbol{Z})|^2}}_{\textit{geometric}}. \tag{4.20}$$

Here,

$$U_d = \frac{\mathrm{d}\ell_d}{\mathrm{d}t} = \frac{\mathrm{Re}(\overline{T(\boldsymbol{Z})} \cdot \mathscr{N}_1(\boldsymbol{Z}))}{|T(\boldsymbol{Z})|^2} \tag{4.21}$$

is the so-called dynamical phase velocity (Simon 1983; Samuel & Bhandari 1988). Since $\overline{T(\mathbf{Z})}\cdot\mathscr{N}_1(\mathbf{Z})$ and $|T(\mathbf{Z})|^2$ are invariant under translation symmetry, ℓ_d can also be determined by replacing $\mathbf{Z}$ with the orbit z in $\mathscr{P}$, which is usually known or observable in applications. Indeed, from (4.2) and (4.21)

$$U_d = \frac{\mathrm{Re}(\overline{T(z)}\cdot\mathscr{N}_1(z))}{|T(z)|^2} = \frac{\mathrm{Re}\left(\overline{T(z)}\cdot\dfrac{\mathrm{d}z}{\mathrm{d}t}\right)}{|T(z)|^2}. \tag{4.22}$$

It is straightforward to show that U_d depends on the evolution of the concentration field c in the fixed laboratory frame (x, t) associated with the orbit z in $\mathscr{P}$. Indeed, since

$$\langle(\partial_x c)^2\rangle_x = \sum_{m=1}^{N} m^2k_0^2|z_m|^2 = |T(z)|^2 \tag{4.23}$$

and

$$\langle\partial_t c\partial_x c\rangle_x = \mathrm{Re}\sum_{m=1}^{N}\mathrm{i}mk_0\overline{z_m}\frac{\mathrm{d}z_m}{\mathrm{d}t} = -\mathrm{Re}\left(\overline{T(z)}\cdot\frac{\mathrm{d}z}{\mathrm{d}t}\right), \tag{4.24}$$

it follows that

$$U_d = -\frac{\langle\partial_t c\partial_x c\rangle_x}{\langle(\partial_x c)^2\rangle_x}. \tag{4.25}$$

Thus, the dynamical phase velocity U_d is the 1D comoving frame, or convective, speed similar to that defined for 2D and 3D concentration fields (see (2.5) and (2.11), respectively). Clearly, U_d also follows by minimization of the spatial mean of the material derivative of c as in (2.4). Further, from (4.20) we define the geometric phase velocity as

$$U_g = \frac{\mathrm{d}\ell_g}{\mathrm{d}t} = -\frac{\mathrm{Re}\left(\overline{T(\mathbf{Z})}\cdot\dfrac{\mathrm{d}\mathbf{Z}}{\mathrm{d}t}\right)}{|T(\mathbf{Z})|^2}. \tag{4.26}$$

Note that U_g and U_d in (4.25) are not the same since $\mathrm{d}\mathbf{Z}/\mathrm{d}t \neq \mathrm{d}z/\mathrm{d}t$ (see (4.2) and (4.13)). Further, in contrast to the dynamical U_d, the geometric U_g cannot be related to the evolution of the concentration field c in the fixed laboratory frame (x, t); it depends only on the shape-changing evolution of the desymmetrized field c_D (see (4.6)) in the symmetry-reduced frame $(x - \ell_d - \ell_g, t)$. Here, we recall that c_D is associated with the desymmetrized orbit $\mathbf{Z}$ in the quotient space $\mathscr{M}$, or base manifold. Indeed, (4.26) can be written as

$$U_g = \frac{\langle\partial_t c_D\partial_x c_D\rangle_x}{\langle(\partial_x c_D)^2\rangle_x}, \tag{4.27}$$

where we have used (4.23) and (4.24) replacing z with $\mathbf{Z}$. Clearly, the geometric phase velocity depends on the arbitrary choice of the Fourier slice S_j. Indeed, different slices yield different desymmetrized concentration fields c_D, as discussed later. Further, different scalar products in (4.19) could be used to filter out the contribution of large or small flow scales leading to different slice representations. As mentioned above, in this work we only consider the standard scalar product and all flow scales are accounted for.

The comoving orbit

$$\mathbf{Z}_d(t) = g_{-\ell_d}(z) \tag{4.28}$$

is the orbit seen from a comoving frame drifting at the speed U_d. In physical space it corresponds to an evolution of the dye concentration in the comoving frame $(x - \ell_d, t)$. Note that in general $\ell_d(t)$ is time varying, and constant only for travelling waves. Clearly, the dynamical drift ℓ_d increases with the time taken by the trajectory $\boldsymbol{z}(t)$ to wander around $\mathscr{P}$. The geometric drift ℓ_g instead depends upon the path $\Gamma = \{Z_n(t)\}$ associated with the desymmetrized orbit $\boldsymbol{Z}(t)$ in the quotient space. Indeed,

$$\ell_g(t) = \int_0^t U_g \,\mathrm{d}\tau = -\int_0^t \frac{\mathrm{Re}\left(\overline{T(\boldsymbol{Z})} \cdot \dfrac{\mathrm{d}\boldsymbol{Z}}{\mathrm{d}\tau}\right)}{|T(\boldsymbol{Z})|^2}\,\mathrm{d}\tau = -\int_\Gamma \frac{\mathrm{Re}(\overline{T(\boldsymbol{Z})} \cdot \mathrm{d}\boldsymbol{Z})}{|T(\boldsymbol{Z})|^2}. \tag{4.29}$$

The desymmetrized orbit $\boldsymbol{Z}$ is obtained by further shifting the comoving orbit $\boldsymbol{Z}_d$ in (4.28) by the geometric drift ℓ_g as

$$\boldsymbol{Z} = g_{-\ell_g}(\boldsymbol{Z}_d) = g_{-\ell_d-\ell_g}(\boldsymbol{z}). \tag{4.30}$$

Different slice representations yield different symmetry-reduced frames $(x - \ell_d - \ell_g, t)$ from which one observes distorted shape-changing dynamics of the dye concentration field. Only relative equilibria or travelling waves have null geometric phase, since their shape is not dynamically changing in the base manifold as they reduce to equilibria. The geometric drift ℓ_g and associated speed U_g can be indirectly computed from (4.15) and (4.17) as $\ell_g = \ell_s - \ell_d$ and $U_g = U_s - U_d$ respectively. The pairs $(\ell_s,\, U_s = \mathrm{d}\ell_s/\mathrm{d}t)$ and $(\ell_d = \int_0^t U_d \,\mathrm{d}\tau,\, U_d)$ are easily estimated from concentration measurements.

The Fourier slice should be properly chosen to provide a physically meaningful symmetry-reduced frame, as discussed in the next section.

4.2. *Symmetry reduction of LIF measurements*

In this section, we present a symmetry reduction of the acquired LIF measurements of turbulent pipe flow (see § 2.1). In particular, we study their evolution in physical space and in the associated state space $\mathscr{P}$ of dimension $N = 40\,430$ equal to the total number of data image pixels (65×622).

Regarding the choice of the Fourier slice S_j, it is in general entirely arbitrary. There is no unique way to quotient out the symmetry. The most likely choice would be S_1, but for our measurements this choice will not produce a physically meaningful symmetry reduction. Higher-order slices are required.

In particular, figures 6 and 7 illustrate the space–time evolution of a passive scalar structure and concentration profiles. Figure 6(*a*) shows the dye concentration $c(x, t)$ at the pipe centreline in the fixed frame (x, t) (see also figure 7). A drift in the streamwise direction x is observed. The corresponding orbit $\boldsymbol{z}(t)$ in the subspace $\{\mathrm{Re}(z_{11}), \mathrm{Im}(z_{13}), \mathrm{Re}(z_{15})\}$ of $\mathscr{P}$ is shown in figure 8(*a*,*d*). Note that the excursion of the orbit while the concentration c lingers above the threshold $0.95c_{max}$ is complicated (bold line) since it wanders around its group orbit as a result of the drift induced by the translation symmetry. Figure 6(*c*) shows the space–time evolution in the comoving frame $(x - \ell_d, t)$. Note that the dye concentration still experiences a significant drift (see also figure 7). As a result, the associated orbit in state space still wanders around the group orbit. A proper choice of the Fourier slice can provide a physically meaningful symmetry-reduced frame. For example, if we choose the first Fourier mode slice S_1, figure 6(*a*) depicts the associated evolution in the symmetry-reduced frame $(x - \ell_d - \ell_g, t)$. Clearly, the symmetry is quotiented out, but in the Fourier slice

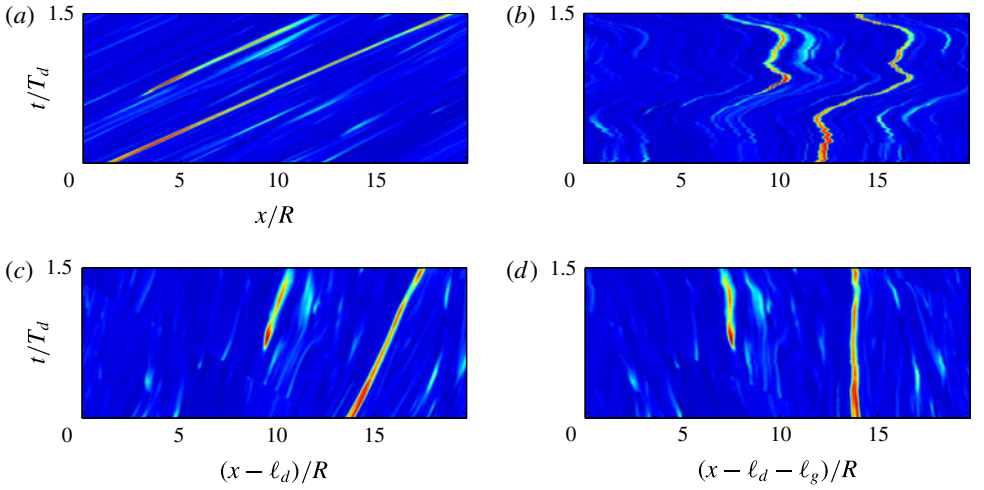

FIGURE 6. (Colour online) Symmetry reduction of LIF measurements: space–time evolution of a passive scalar structures: (*a*,*c*) measured concentration $C(x,\, y=0,\, t)$ at the pipe centreline in the (*a*) fixed frame, (*c*) comoving frame $(x-\ell_d,\, t)$; (*b*,*d*) symmetry-reduced frame $(x-\ell_d-\ell_g,\, t)$ using Fourier slices (*b*) S_1 and (*d*) S_{25}; time average $\overline{U}_d \approx 6.74$ cm s^{-1}, $\overline{U}_g \approx 0.4U_d$ and $T_d = \overline{U}_d/R$.

S_1 we observe a distorted shape-changing dynamics of the dye concentration. Instead, if we choose the Fourier slice S_{25} the drift almost disappears in the corresponding symmetry-reduced frame, as shown in figure 6(*c*) (see also figure 7). Here, this slice is sufficient to symmetry-reduce the orbit $\boldsymbol{z}$ over the analyzed time span as its Fourier components z_k, with $k \sim 20$–30, never linger near zero, whereas smaller or larger wavenumber modes can be small. The corresponding symmetry-reduced orbits $\boldsymbol{Z}(t)$ associated with S_1 and S_{25} are computed from (4.4). Their time evolutions within the subspace $\{\mathrm{Re}(Z_{11}), \mathrm{Im}(Z_{13}), \mathrm{Re}(Z_{15})\}$ of $\mathscr{M}$ are shown in figure 8(*b*,*e*) and figure 8(*c*,*f*) respectively. Here, the excursion of the orbits while the concentration c is high ($>0.95c_{max}$) is marked as a bold line. Similar dynamics is also observed when projecting the orbits onto the subspace of their respective most energetic proper orthogonal decomposition (POD) modes, as shown in figure 9. The POD projection of the symmetry-reduced orbit $\boldsymbol{Z}$ is performed within the corresponding symmetry-reduced space. Note that any two POD mode amplitudes are statistically uncorrelated by construction as are any two components Z_p and Z_q chosen at random. Clearly, this does not imply that they are stochastically independent since they evolve on the quotient manifold $\mathscr{M}$, which is unknown. As an example, consider two random variables X and Y that satisfy $X^2 + Y^2 - 1 = 0$. They are uncorrelated but not independent and POD projections will not help in revealing the intrinsic manifold structure. Local linear embedding techniques may be more appropriate and appealing (Roweis & Saul 2000), but they are beyond the scope of our work.

Figure 10(*a*,*c*) shows that geometric drifts associated with Fourier slices S_1 and S_{25} are different and so are the respective geometric phase velocities (see figure 10*b*,*d*). Clearly, the dynamical component U_d is the same since it does not depend on the symmetry-reduction scheme or slice. Note that ℓ_g is not the drift seen by an observer in the symmetry-reduced frame. If it were, the geometric phase velocity associated with the slice S_{25} would be zero since the desymmetrized dye concentration field

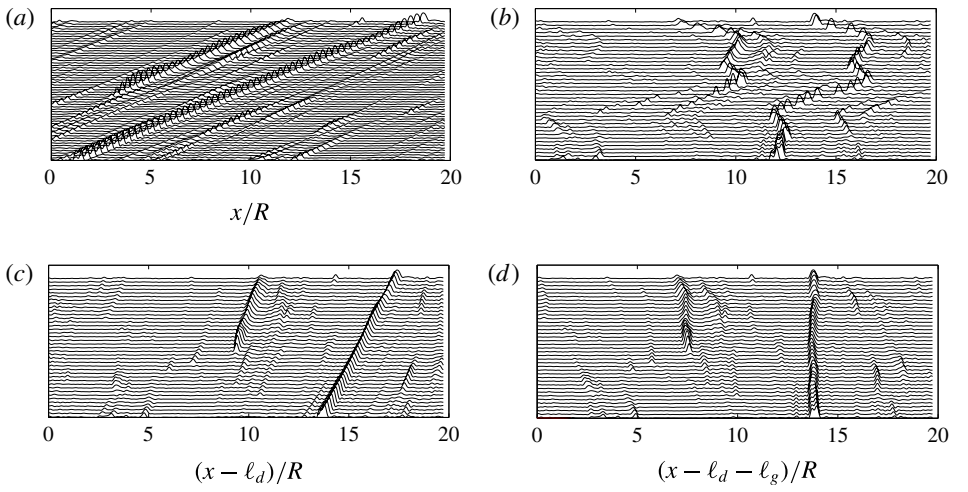

FIGURE 7. Symmetry reduction of LIF measurements: (*a*,*c*) concentration profiles at increasing instants of time of the measured concentration $c(x,\, y = 0,\, t)$ at the pipe centreline in the (*a*) fixed frame, (*c*) comoving frame $(x - \ell_d,\, t)$; (*b*,*d*) symmetry-reduced frame $(x - \ell_d - \ell_g,\, t)$ using Fourier slices (*b*) S_1 and (*d*) S_{25}. In each plot time increases from bottom to top. Associated 2D patterns are shown in figure 6).

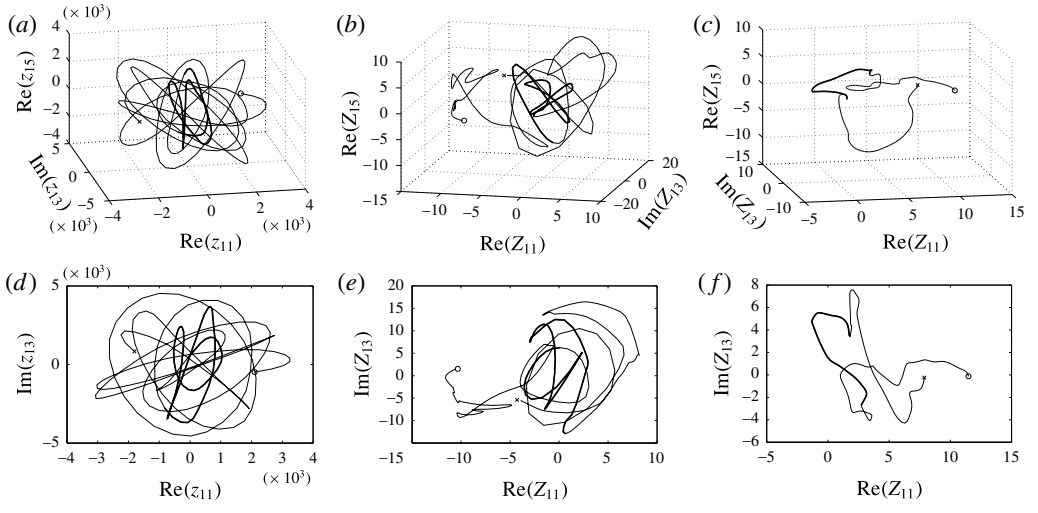

FIGURE 8. Symmetry reduction of LIF measurements: (*a*,*d*) orbit trajectory $\boldsymbol{z}$ in the subspace $\{\mathrm{Re}(z_{11}),\, \mathrm{Im}(z_{13}),\, \mathrm{Re}(z_{15})\}$ of the state space $\mathscr{P}$ associated with the passive scalar dynamics in the lab frame of figure 7 (see also figure 6); and corresponding symmetry-reduced orbits $\boldsymbol{Z}$ in the subspace $\{\mathrm{Re}(Z_{11}),\, \mathrm{Im}(Z_{13}),\, \mathrm{Re}(Z_{15})\}$ of the base manifold $\mathscr{M}$ associated with Fourier slices (*b*,*e*) S_1 and (*c*,*f*) S_{25}. The bold line indicates the excursion of the orbit while the concentration c lingers above the threshold $0.95c_{max}$ ($\bigcirc$ = initial time, $\times$ = final time).

does not drift. If the same observer drifts by ℓ_g he will observe the dynamics in the comoving frame. This explains why the geometric phase velocity U_g associated with the slice S_1 is negative in the time span $0.5 < t/T_d < 1$. With reference to figure 7, in

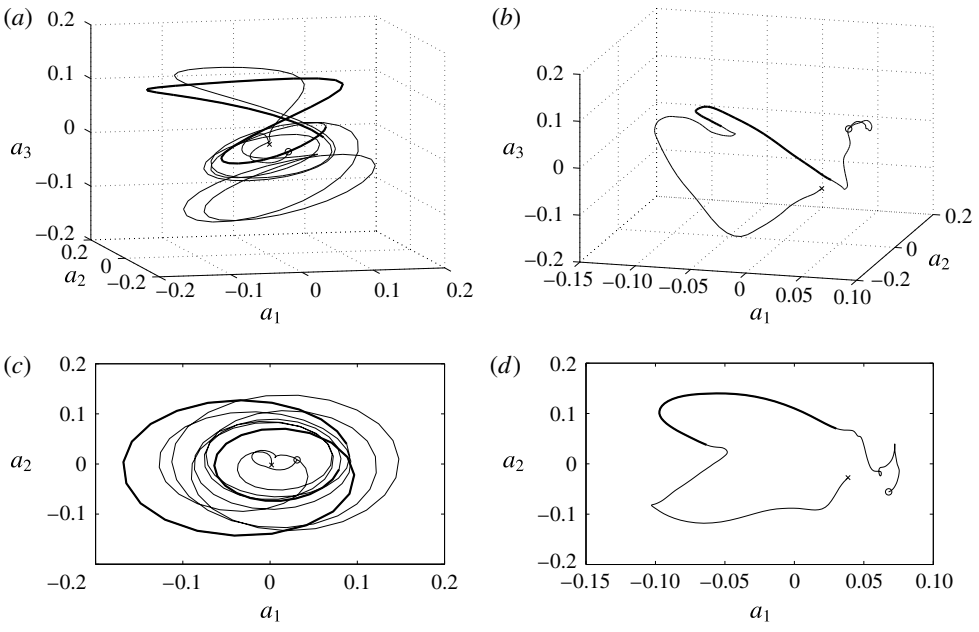

FIGURE 9. Symmetry reduction of LIF measurements: (*a*,*c*) orbit trajectories $\boldsymbol{z}$ associated with the passive scalar dynamics in the lab frame (see figure 6*a*) projected onto the subspace (a_1, a_2, a_3) of the most energetic POD modes; (*b*,*d*) corresponding desymmetrized orbit $\boldsymbol{Z}$ in the symmetry-reduced frame associated with the Fourier slice S_{25}. The bold line indicates the excursion of the orbit while the concentration c lingers above the threshold $0.95c_{max}$ ($\bigcirc$ = initial time, $\times$ = final time).

that time interval an observer in the symmetry-reduced frame needs to decelerate in order to follow the dye concentration evolution seen in the comoving frame.

The observed speed u of dye concentration peaks is approximately 40 % larger than the comoving frame velocity U_d, which changes slightly during the event. The excess speed $\delta u = u - U_d$ is fairly well explained by the geometric phase velocity $U_g \approx 0.4U_d$ associated with slice S_{25}, as seen in figure 10(*d*). This appears to be a general trend of the flow as can be seen in figure 11, which shows the observed normalized speed u/U_d of dye concentration peaks tracked in space as a function of their amplitude c/C_{max}, and the associated probability density function, where C_{max} denotes the observed maximum value of dye concentration over the whole data set. As the peak amplitude increases, their speed u tends to $1.43U_d$. Furthermore, in the symmetry-reduced frame, we observe the shape-changing dynamics of passive scalar structures (see figure 7*d*). This induces the 'self-propulsion velocity' U_g of the flow structures similar to that of the motion of a swimmer at low Reynolds numbers (Shapere & Wilczek 1989). Only when the geometric velocity $U_g \ll U_d$ is Taylor's approximation valid and as a result the flow structures slightly deform as they are advected at the comoving frame or dynamical phase velocity U_d, which is close to the mean flow U_m.

5. Conclusions

We have presented a Fourier-based symmetry-reduction scheme for dynamical systems with continuous translation symmetries. As an application, we have

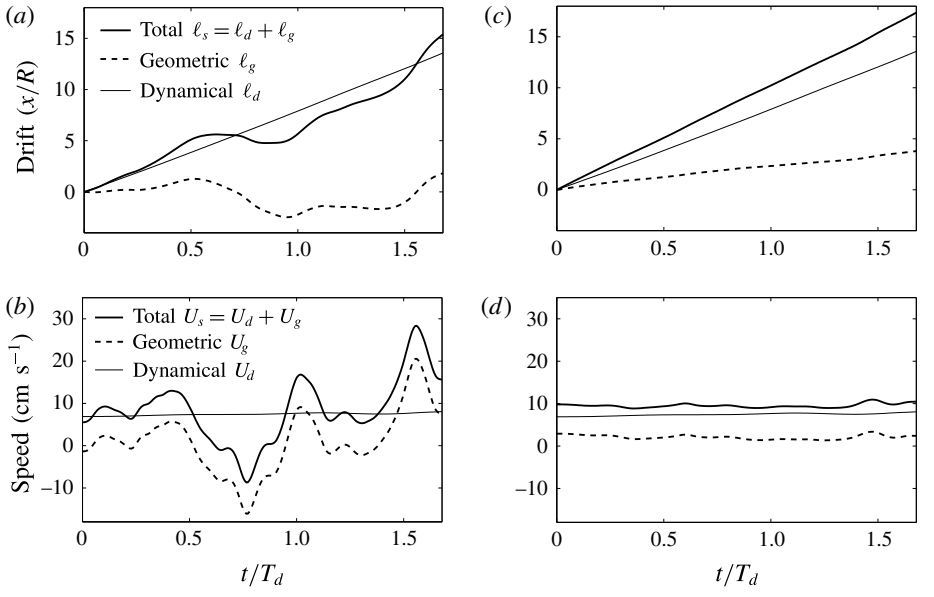

FIGURE 10. Symmetry reduction of LIF data using Fourier slice S_1 (*a*,*b*) and S_{25} (*c*,*d*); (*a*,*c*) total, dynamical and geometric drifts and (*b*,*d*) corresponding velocities U_s, U_d and U_g associated with the orbit in state space of figure 8.

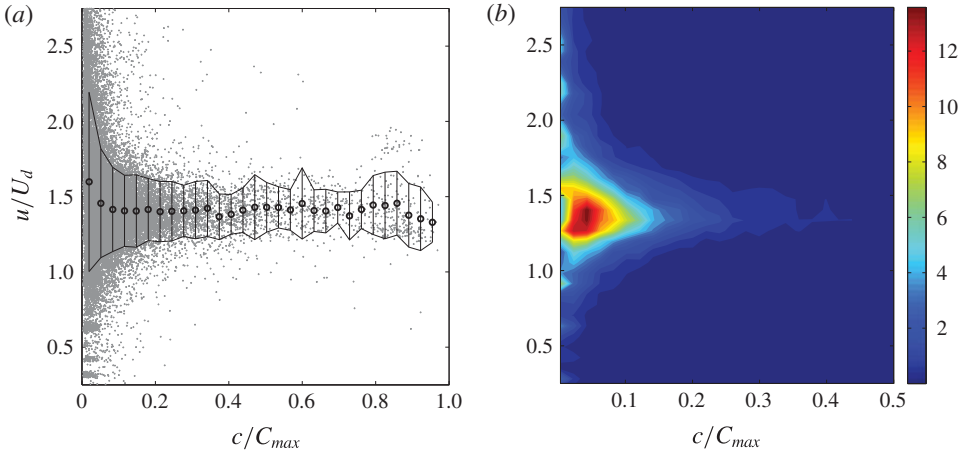

FIGURE 11. (Colour online) LIF experiments: (*a*) observed normalized dye concentration peak speed u/U_d as a function of the amplitude peak c/C_{max}, and (*b*) associated probability density function, with C_{max} denoting the observed maximum value of dye concentration over the whole data set.

symmetry-reduced LIF measurements of fluorescent dye concentration fields tracing a turbulent pipe flow at Reynolds number $Re = 3200$. The symmetry reduction of LIF data on higher-order Fourier slices revealed that the motion of passive scalar structures is associated with the dynamical and geometric phases of the corresponding orbits in state space. In particular, the observed speed $u \approx 1.43U_d$

of dye concentration peaks exceeds the comoving or convective velocity U_d. A physically meaningful representation of the quotient space by a proper choice of the Fourier slice explains the excess speed $\delta u = u - U_d$ as the geometric phase velocity $U_g \approx 0.43 U_d$ associated with the Fourier slice S_{25}. Similar to the motion of a swimmer at low Reynolds number, the excess speed δu is a 'self-propulsion' velocity U_g induced by the shape-changing dynamics of passive scalar structures as revealed in the symmetry-reduced frame.

Symmetry reduction is promising for the analysis of 3D LIF and particle image velocimetry (PIV) measurements as well as simulate flows of pipe turbulence, in order to unveil the 'shape of turbulence' and the hidden skeleton of its chaotic dynamics in state space. Further, the dependence of geometric phase velocities on the Reynolds number may shed some light on the nature of transition to turbulence, since the geometric phase is a measure of the curvature of the quotient manifold.

Acknowledgements

F.F. acknowledges the Georgia Tech graduate courses 'Classical Mechanics II' taught by J. Bellissard in Spring 2013 and 'Nonlinear dynamics: Chaos, and what to do about it?' taught by P. Cvitanović in Spring 2012. F.F. also thanks A. Shapere for discussions on geometric phases, and F. Bonetto, N. B. Budanur, B. Eckhardt, M. Farazmand, C. Zeng as well as E. Siminos for discussions on symmetry reduction.

Appendix A

The time derivative of $z = g_{\ell_s}(\mathbf{Z})$ is

$$\frac{\mathrm{d}z}{\mathrm{d}t} = g_{\ell_s}\left(\frac{\mathrm{d}\mathbf{Z}}{\mathrm{d}t}\right) + \frac{\mathrm{d}\ell_s}{\mathrm{d}t}(\partial_{\ell_s} g)\mathbf{Z}, \tag{A 1}$$

and the governing equation (4.2) for z yields

$$g_{\ell_s}\left(\frac{\mathrm{d}\mathbf{Z}}{\mathrm{d}t}\right) + \frac{\mathrm{d}\ell_s}{\mathrm{d}t}(\partial_{\ell_s} g)\mathbf{Z} - \mathscr{N}_1(g_{\ell_s}\mathbf{Z}) = 0, \tag{A 2}$$

where the dependence of $\mathscr{N}_1$ on c_0 and $\hat{\boldsymbol{v}}$ is dropped for clarity of notation. Factoring out g_{ℓ_s} yields

$$g_{\ell_s}\left(\frac{\mathrm{d}\ell_s}{\mathrm{d}t}\underbrace{g_{\ell_s}^{-1}(\partial_{\ell_s} g)\mathbf{Z}}_{T(\mathbf{Z})} + \frac{\mathrm{d}\mathbf{Z}}{\mathrm{d}t} - \underbrace{g_{\ell_s}^{-1}\mathscr{N}_1(g_{\ell_s}\mathbf{Z})}_{\mathscr{N}_1(\mathbf{Z})}\right) = 0. \tag{A 3}$$

This can be further simplified using (4.14) and noting that $\mathscr{N}_1$ is invariant under translation symmetry, that is

$$g_{\ell_s}\left(\frac{\mathrm{d}\mathbf{Z}}{\mathrm{d}t} + \frac{\mathrm{d}\ell_s}{\mathrm{d}t}T(\mathbf{Z}) - \mathscr{N}_1(\mathbf{Z})\right) = 0. \tag{A 4}$$

For translation symmetries, $g_{\ell_s}(q) = 0$ if and only if $q = 0$, thus the evolution of $\mathbf{Z}$ is governed by

$$\frac{\mathrm{d}\mathbf{Z}}{\mathrm{d}t} + \frac{\mathrm{d}\ell_s}{\mathrm{d}t}T(\mathbf{Z}) - \mathscr{N}_1(\mathbf{Z}) = 0. \tag{A 5}$$

REFERENCES

BANNER, M. L., BARTHELEMY, X., FEDELE, F., ALLIS, M., BENETAZZO, A., DIAS, F. & PEIRSON, W. L. 2014 Linking reduced breaking crest speeds to unsteady nonlinear water wave group behavior. *Phys. Rev. Lett.* **112**, 114502.

BERRY, M. V. 1984 Quantal phase factors accompanying adiabatic changes. *Proc. R. Soc. Lond.* A **392** (1802), 45–57.

BUDANUR, N. B., CVITANOVIĆ, P., DAVIDCHACK, R. L. & SIMINOS, E. 2015 Reduction of so(2) symmetry for spatially extended dynamical systems. *Phys. Rev. Lett.* **114**, 084102.

CHANDLER, G. J. & KERSWELL, R. R. 2013 Invariant recurrent solutions embedded in a turbulent two-dimensional Kolmogorov flow. *J. Fluid Mech.* **722**, 554–595.

CVITANOVIĆ, P. 2013 Recurrent flows: the clockwork behind turbulence. *J. Fluid Mech.* **726**, 1–4.

CVITANOVIĆ, P., ARTUSO, R., MAINIERI, R., TANNER, G. & VATTAY, G. 2012 *Chaos: Classical and Quantum*. Niels Bohr Institute, Copenhagen, www.ChaosBook.org.

CVITANOVIĆ, P. & ECKHARDT, B. 1991 Periodic orbit expansions for classical smooth flows. *J. Phys. A: Math. Gen.* **24** (5), L237.

CVITANOVIĆ, P. P., BORRERO-ECHEVERRY, D., CARROLL, K. M., ROBBINS, B. & SIMINOS, E. 2012 Cartography of high-dimensional flows: a visual guide to sections and slices. *Chaos* **22**, 047506.

DEL ÁLAMO, J. C. & JIMENEZ, J. 2009 Estimation of turbulent convection velocities and corrections to Taylor's approximation. *J. Fluid Mech.* **640**, 5–26.

FAISST, H. & ECKHARDT, B. 2003 Traveling waves in pipe flow. *Phys. Rev. Lett.* **91** (22), 224502.

FEDELE, F. 2014*a* Geometric phases of water waves. *Europhys. Lett.* **107** (69001).

FEDELE, F. 2014*b* On certain properties of the compact Zakharov equation. *J. Fluid Mech.* **748**, 692–711.

FROEHLICH, S. & CVITANOVIĆ, P. 2012 Reduction of continuous symmetries of chaotic flows by the method of slices. *Commun. Nonlinear Sci. Numer. Simul.* **17** (5), 2074–2084.

GIBSON, J. F., HALCROW, J. & CVITANOVIĆ, P. 2008 Visualizing the geometry of state space in plane Couette flow. *J. Fluid Mech.* **611**, 107–130.

GRITSUN, A. 2011 Connection of periodic orbits and variability patterns of circulation for the barotropic model of atmospheric dynamics. *Dokl. Earth Sci.* **438** (1), 636–640.

GRITSUN, A. 2013 Statistical characteristics, circulation regimes and unstable periodic orbits of a barotropic atmospheric model. *Phil. Trans. R. Soc. Lond.* A **371** (1991).

HANNAY, J. H. 1985 Angle variable holonomy in adiabatic excursion of an integrable hamiltonian. *J. Phys. A: Math. Gen.* **18** (2), 221.

HOPF, H. 1931 Über die abbildungen der dreidimensionalen sphäre auf die kugelfläche. *Math. Ann.* **104** (1), 637–665.

HUSEMÖLLER, D. 1994 *Graduate Texts in Mathematics, 20*, 3rd edn., vol. 1. Springer.

KREILOS, T., ZAMMERT, S. & ECKHARDT, B. 2014 Comoving frames and symmetry-related motions in parallel shear flows. *J. Fluid Mech.* **751**, 685–697.

KROGSTAD, P.-Å., KASPERSEN, J. H. & RIMESTAD, S. 1998 Convection velocities in a turbulent boundary layer. *Phys. Fluids* **10** (4), 949–957.

PANCHARATNAM, S. 1956 Generalized theory of interference, and its applications. *Proc. Indian Acad. Sci.* A **44** (5), 247–262.

ROWEIS, S. T. & SAUL, L. K. 2000 Nonlinear dimensionality reduction by locally linear embedding. *Science* **290** (5500), 2323–2326.

ROWLEY, C. W., KEVREKIDIS, I. G., MARSDEN, J. E. & LUST, K. 2003 Reduction and reconstruction for self-similar dynamical systems. *Nonlinearity* **16** (4), 1257.

ROWLEY, C. W. & MARSDEN, J. E. 2000 Reconstruction equations and the Karhunen–Loève expansion for systems with symmetry. *Physica* D **142** (1–2), 1–19.

SAMUEL, J. & BHANDARI, R. 1988 General setting for Berry's phase. *Phys. Rev. Lett.* **60**, 2339–2342.

SHAPERE, A. & WILCZEK, F. 1989 Geometry of self-propulsion at low Reynolds number. *J. Fluid Mech.* **198**, 557–585.

SIMINOS, E. & CVITANOVIĆ, P. 2011 Continuous symmetry reduction and return maps for high-dimensional flows. *Physica* D **240** (2), 187–198.

SIMON, B. 1983 Holonomy, the quantum adiabatic theorem, and Berry's phase. *Phys. Rev. Lett.* **51** (24), 2167–2170.

STEENROD, N. 1999 *The Topology of Fibre Bundles*. Princeton University Press.

TAYLOR, G. I. 1938 The spectrum of turbulence. *Proc. R. Soc. Lond.* A **164** (919), 476–490.

TIAN, X. & ROBERTS, P. J. 2003 A 3D lif system for turbulent buoyant jet flows. *Exp. Fluids* **35** (6), 636–647.

VISWANATH, D. 2007 Recurrent motions within plane Couette turbulence. *J. Fluid Mech.* **580**, 339–358.

WEDIN, H. & KERSWELL, R. R. 2004 Exact coherent structures in pipe flow: travelling wave solutions. *J. Fluid Mech.* **508**, 333–371.

WILLIS, A. P., CVITANOVIĆ, P. & AVILA, M. 2013 Revealing the state space of turbulent pipe flow by symmetry reduction. *J. Fluid Mech.* **721**, 514–540.